Article

Optical Mie Scattering by DNA-Assembled Three-Dimensional Gold Nanoparticle Superlattice Crystals

Haobijam Johnson Singh, Doxi Misatziou, Callum Wheeler, Álvaro Buendía, Vincenzo Giannini, José A. Sánchez-Gil, Martinus H. V. Werts, Tom Brown, Afaf H. El-Sagheer, Antonios G. Kanaras,* and Otto L. Muskens*

Cite This: ACS Appl. Opt. Mater. 2023, 1, 69−77

Read Online

ACCESS | Metrics & More | Article Recommendations | SI Supporting Information

ABSTRACT: Programmable assemblies of gold nanoparticles engineered with DNA have intriguing optical properties such as Coulomb-interaction-driven strong coupling, polaritonic response in the visible range, and ultralow dispersion dielectric response in the infrared spectral range. In this work, we demonstrate the optical Mie resonances of individual microcrystals of DNA−gold nanoparticle superlattices. Broadband hyperspectral mapping of both transmission and dark-field scattering reveal a polarization-insensitive optical response with distinct spectral features in the visible and near-infrared ranges. Experimental observations are supported by numerical simulations of the microcrystals under a resonant effective medium approximation in the regime of capacitively coupled nanoparticles. The study identifies a universal characteristic optical response which is defined by a band of multipolar Mie resonances, which only weakly depend on the crystal size and light polarization. The use of gold superlattice microcrystals as scattering materials is of interest for fields such as complex nanophotonics, thermoplasmonics, photocatalysis, sensing, and nonlinear optics.

KEYWORDS: Colloidal Nanoparticles, DNA, Crystals, Optical Properties, Hyperspectral Imaging, DNA Assembly, Supercrystals
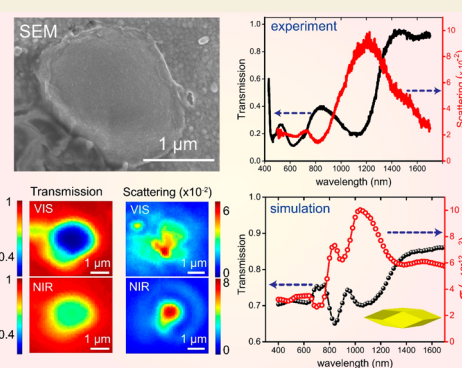
INTRODUCTION

Programmable configuration of materials at the nanoscale is central for the development of new photonic devices and their applications in many fields such as biochemical sensing, imaging, therapeutics, photovoltaics, photocatalysis, and photodetection.[1,2] Control of the bottom-up assembly of metallic nanoparticles (NPs) is an attractive approach to realize and master the collective optical properties of matter. Metallic NPs can redirect propagating electromagnetic radiation and transfer it into strongly enhanced localized subwavelength modes at the nanoscale through the excitation of localized surface plasmon resonances (LSPRs).[3,4] Assembly of metallic NPs into mesoscale structures offers an attractive approach to achieving new photonic functionalities exploiting the electromagnetic coupling among constituent particles for light control and manipulation and has been used for the fabrication of optically active metamaterials and metasurfaces.[4−9] Plasmonic assemblies can exhibit unusual optical properties such as near-zero permittivity,[10−12] negative refractive index,[13,14] polaritonic and strong coupling effects,[7,15] chirality,[16−19] local field enhancement,[20−22] nonlinearity,[23,24] and lasing.[8,25]

Typically, lithographic top-down approaches have been widely used to fabricate optical metamaterials and metasurfaces.[26,27] While this strategy is efficient and well-explored,

it has limitations, for example, in the design of three-dimensional (3D) structures,[26,28] prompting the need for complementary approaches enabling the fabrication of more complex optical metamaterials for ultracompact next-generation photonic device applications.[29−31] Bottom-up, DNA-based assembly approaches indeed yielded new types of 3D metamaterials[32−35] and have been shown to serve as a versatile strategy for creating programmable self-assembly of nanoparticles, yielding superstructures exhibiting unique optical properties.[36−38] Previous studies of such 3D materials have already revealed intriguing properties such as near-zero permittivity,[39] photonic band gaps,[40] unconventional optical scattering,[36,37] and high refractive index in the mid-infrared range.[38] Since 2008, when for the first time DNA-functionalized gold nanoparticles were assembled into large 3D superlattices with body-centered cubic (bcc) and face-centered cubic (fcc) lattice configurations,[33,34] DNA design[35,41,42] has
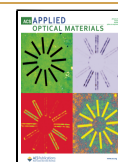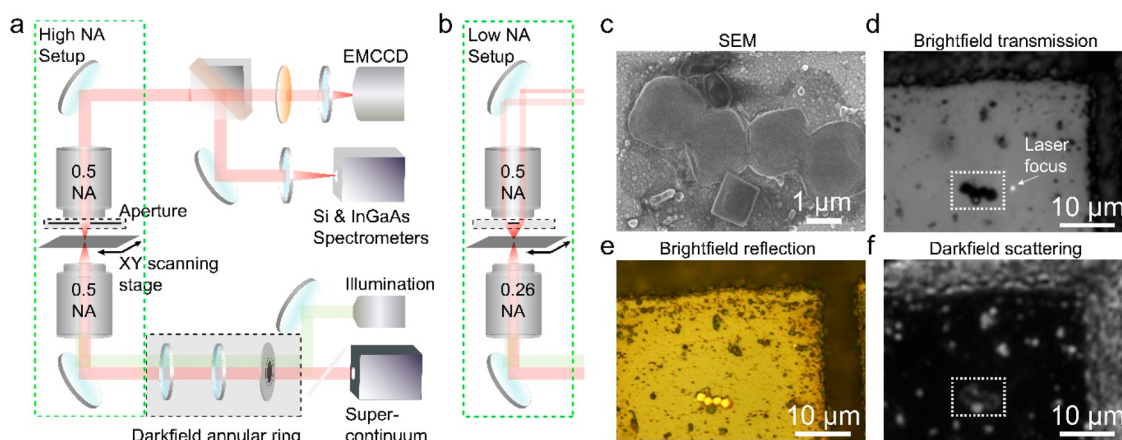
Figure 1. Optical setup and correlated SEM optical imaging. (a) Schematic of the optical setup for hyperspectral scanning microscopy showing light sources, double 0.5 NA transmission microscope ("high NA" setup), imaging, and detection paths. Shaded regions include dark-field annulus with relay lenses and matching aperture stop. (b) Details of the modified setup involving a 0.2 NA illumination objective and matched aperture stop for dark-field imaging at low-angle excitation ("low NA" setup). (c) SEM image of cluster of AuSLs. (d) Bright-field transmission, (e) reflection, and (f) dark-field scattering used for colocalization of optical image with the SEM region. Dashed rectangle in (d,f) denotes scan area for hyperspectral imaging. Bright spot in (d) is the focus of the supercontinuum light source.

enabled the elaboration of a rich library of nanoparticle superlattices, consisting of nanoparticles of various size,[43] shape,[44] and composition.[39,45−49] The ability to combine and control the assembly of a variety of nanoparticles into desired 3D structures has allowed the construction of new designer nanomaterials[50] for applications in electronics,[51] catalysis,[52] and optics.[16,53,54]

Experimental[38] as well as theoretical[37,55] studies on the optical properties of nanoparticle superlattices have recently been reported, focusing on colloidal crystals assembled from large-size gold nanocubes. DNA-mediated assembly of nanocubes results in a simple cubic lattice symmetry,[38] which allows exploiting the very strong capacitive coupling and the intense electric and magnetic fields that exist between flat facets of neighboring nanocubes[22,56,57] to design optical metamaterials with unique properties. Large nanocubes assembled into microcrystals were shown to exhibit strong Mie resonances in the mid-infrared range.[38] In comparison, crystals assembled with spherical-shape nanoparticles can result in fcc as well as bcc symmetry.[34] Despite lacking the strong capacitive coupling of nanocubes, earlier works on colloidal crystals with spherical particles have also revealed an optical response governed by strong light−matter interaction. For instance, Turek et al. experimentally studied the optical response of their spherical supercluster metamaterials in the visible range and demonstrated their use in surface-enhanced Raman scattering applications.[21] Reich et al. explored light−matter coupling between surface plasmons and continuum of photons into polaritonic modes in the strong coupling regime in the visible part of the spectrum.[7] Both of these works make use of larger-size spherical nanoparticles (43 nm in ref [21] and 25−59 nm in ref [7]) and used non-DNA-based self-assembly approaches to fabricate their respective superlattices. Experimental studies on such superlattices are still very limited, and a detailed spectroscopic investigation especially of crystals assembled from small sizes (∼10−15 nm) and closed-packed spherical nanoparticles covering the entire visible−near-IR range is lacking.

Here, we report an experimental investigation of the optical response of three-dimensional gold NP superlattice crystals obtained via DNA-mediated assembly. We use a multimodal hyperspectral imaging technique[58] with optical transmission (bright-field) and light-scattering (dark-field) microscopy to explore extinction and scattering over a wide spectral range covering the visible and near-infrared spectral range from 400 to 1700 nm. This technique enables us to reliably measure optical response down to individual superlattice microcrystals. Optical spectra of the individual microcrystals are correlated with scanning electron microscopy (SEM) as well as atomic force microscopy studies. Detailed numerical simulations are used to confirm the multipolar nature of the modes, which depend only weakly on polarization or superlattice crystal size.

In our experiments, we synthesized spherical gold nanoparticles (AuNPs) in aqueous solution with an average diameter of 15 nm (Supporting Information, Figure S1) and subsequently functionalized them with oligonucleotides. Following previously established protocols,[59−62] we produced microcrystals of superlattices (AuSLs) comprising AuNPs functionalized with single-stranded DNA that contain 3-cyanovinyl carbazole nucleobase chemical modifications.[63,64] After hybridization with a complementary DNA strand, the 3-cyanovinyl carbazole group can react photochemically with an adjacent thymine nucleobase, forming a covalent bond between the two complementary DNA strands. Thus, the as-synthesized AuSLs were photochemically cross-linked in order to increase the stability of the crystals and were subsequently purified by centrifugation, followed by removal of the supernatant and resuspension of the pellet in Milli-Q water. Detailed experimental structural studies on the functionalized AuSLs using small-angle X-ray scattering were reported elsewhere, and these clearly revealed the bcc arrangement[62] and an edge to edge gap between AuNPs of about 10 nm in the carbazole cross-linked AuSL crystals.[63] To perform correlated electron microscopy and optical studies of single microcrystals, a small amount (20 μL) of the redispersed solution was drop-cast onto an aluminum-doped zinc oxide (AZO)-coated gridded glass slide and left to dry overnight. The AuSLs were then characterized by SEM in order to identify structures for optical studies. Correlated SEM and optical studies are challenging as they require careful exposure and absence of additional conductive film to avoid modification of the sample which could affect the optical response. The use of AZO-
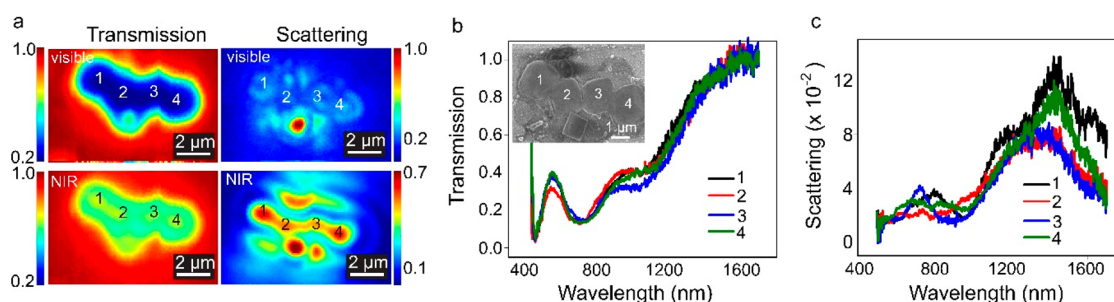
Figure 2. Hyperspectral maps and spectra of cluster of AuSLs. (a) Hyperspectral maps corresponding to transmittance (left column) and scattering (right column) spectra averaged over visible (440−850 nm) and near-IR (850−1650 nm) wavelength bands. (b) Transmittance and (c) scattering spectra as a function of wavelength corresponding to crystals 1−4. These maps were generated for vertically polarized light focused onto the sample plane, scanned in steps of 100 nm. Scattering spectra are scaled relative to the incident dark-field illumination intensity. Inset b: SEM image of AuSLs, scale bar 1 μm.

coated slides reduced charging during SEM and hence allowed imaging of crystals without requiring deposition of additional conducting coatings. Selected structures were characterized further using atomic force microscopy (Supporting Information, Figure S6). The height of individual crystals ranged between 300 and 500 nm, while the in-plane size was typically on the order of 1−2 μm.

AuSLs were characterized optically using a hyperspectral microscopy setup for both transmission (bright-field) and forward scattering (dark-field) configurations. The setup is schematically shown in Figure 1a and consists of two long-working distance, infrared-corrected microscope objectives (Mitutoyo) with a numerical aperture (NA) of 0.5, a supercontinuum light source and visible and near-infrared spectrometers (Andor Shamrock/iDus). The supercontinuum light source produced a collimated beam of unpolarized light covering 380−2300 nm in wavelength, which was attenuated to <1 mW total power on the sample to reduce thermal stress on the crystals. A linear polarizer placed just before the focusing objective controlled the polarization of the incident light. An extended white light source was used to locate the superlattices onto an EMCCD camera (Andor). For dark-field measurements, a dark-field annulus and two relay lenses were introduced in the beam path. An adjustable aperture stop blocks the direct light transmitted through the sample and ensures that only the scattered light from the sample is collected. The measured forward scattering intensity at each wavelength was scaled relative to the measured incident dark-field illumination intensity measured at a location away from the AuSL, with the annular illumination ring in place but without the top aperture stop, hence transmitting the full incident illumination light to the spectrometer. The resulting normalized scattering spectra can be compared to theoretically determined scattering spectra resulting from single microcrystal optical cross section calculations, as shown further below. The sample was mounted on a computer-controlled motorized stage to allow spatial mapping with 100 nm resolution.

Figure 1c−f shows an example of correlated SEM and optical images for a cluster of four AuSLs. The SEM reveals the detailed in-plane structural information on this cluster (Supporting Information, Figure S5 for high-magnification detail of a typical AuSL and Figure S7 for a higher-resolution image of the particular cluster under study). The square object below the crystals is a NaCl crystal originating from the supernatant, which is a feature regularly seen in our samples.

These and other debris surrounding the AuSLs are not taken into consideration in our analysis. Bright-field transmittance and the dark-field scattering image shown in Figure 1d,f help localize the structure and identify the scan area for further hyperspectral study, as indicated by the dashed rectangle. Bright-field reflection (Figure 1e) was taken using another commercial microscopy setup (Zeiss) and reveals a markedly different contrast between the AuSLs, the translucent salt crystals, and other non-AuSL objects present on the sample.

Hyperspectral maps were generated by scanning the sample over a region of interest containing the AuSLs. Figure 2a shows maps of the transmittance and scattering intensity, averaged over spectral bands in the visible (440−850 nm) and NIR (850−1650 nm) regions. These hyperspectral maps reproduce the bright-field and dark-field images (scanned region) in Figure 1d,f but now encoded with full spectral information. We note that while the transmission map shows a near-diffraction-limited performance, the point spread function for the annular illumination dark-field configuration has a smaller central spot but more pronounced side lobe oscillations.[65]

Figure 2b,c shows corresponding spectra extracted from the maps for the four AuSLs labeled 1−4. The results overall reveal strong extinction (low transmittance) in the visible range and reduced extinction (high transmission) in the NIR range. The transmittance spectra show several dips in transmittance occurring at 1100, 750, and 450 nm for all four crystals under study. Scattering spectra reveal a main maximum with up to 12% of scattering in the range of 1200−1600 nm, with a second weaker band in the range of 700−900 nm. While some variation between the AuSLs is seen, the general shape and trends of the spectral features are very similar for the different crystals.

Figure 3 presents more detailed and polarization-dependent studies for selected AuSLs and clusters of crystals. Small micrometer differences in registration between bright-field and dark-field maps are a result of the additional relay lenses placed in the setup. The crystal position is re-established in the maps, as indicated by labels (i) and (ii). Spectral response at these locations is shown in the corresponding panels below the maps. Again, similar features are observed for all crystals, with a particularly pronounced transmission dip at 1150 nm wavelength for the AuSLs in Figure 3a,b,d. Generally, the polarization studies reveal little to no change in the optical spectra of the AuSL upon changing the polarization of the illumination. Stronger scattering in the infrared region is generally observed, and the position of its maximum is found
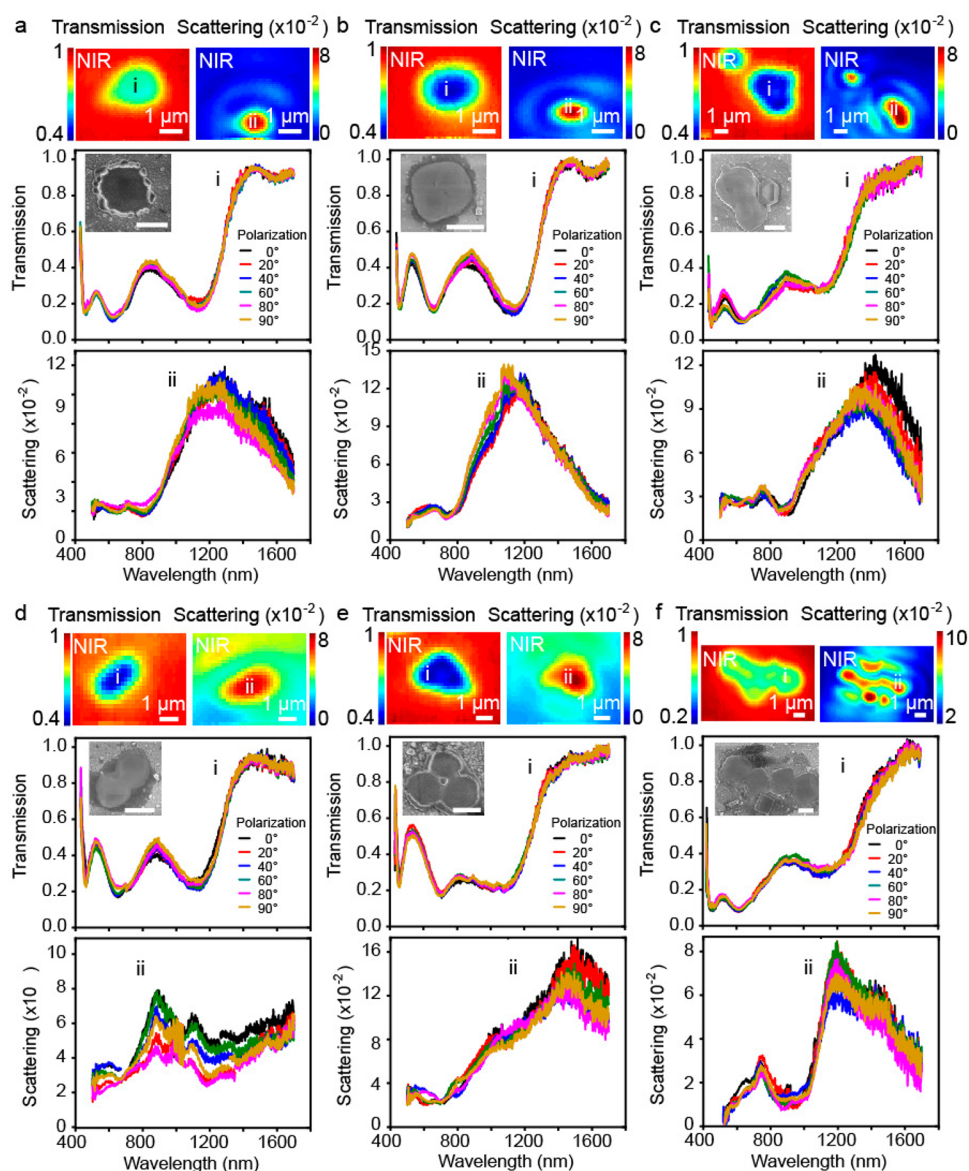
Figure 3. Polarization studies of different microcrystals. (a−f) Studies showing NIR maps (integrated over 850−1650 nm) of transmission and scattering, with spectral response of transmittance and relative scattering intensity at coordinates (i) and (ii) indicated in the maps. Polarization was varied between vertical (0°) and horizontal (90°) (see legend). Corresponding SEM images are shown in the insets. Scale bar corresponds to 1 μm.

to be red-shifted compared to the transmission dips for most of the AuSLs. This behavior is maintained for even more complex AuSL assemblies, such as that shown in Supporting Information Figure S10.

An experimental aspect of importance is the potential impact of laser irradiation upon the AuSL structure. The delicate and soft nature of DNA-assembled AuSLs renders the structure particularly susceptible to damage during measurement. The incident laser power was kept at a sub-mW level to limit energy deposited in the crystal. To check the robustness of the superlattice at these incident power levels, we inspected the crystals in SEM after measurements, as shown in the Supporting Information, Figures S8 and S9. While the overall morphology of the AuSLs remains intact, there appear to be some changes on the surface and edges of the structure. A redistribution is observed of the residue around the AuSLs attributed to various deposits from the buffer solution. The remeasured spectral responses generally look almost identical

to the first measurement but with slight shifts in resonance positions while still maintaining its insensitiveness to input polarization.

Numerical simulations were performed to provide an explanation of the key features seen in the experimental optical spectroscopic response of the AuSLs. Given the small diameters of the AuNPs (∼15 nm) and relatively large interparticle gaps (∼10 nm) of the constituent Au nanospheres of our superlattice, a dipole−dipole coupling among the individual AuNPs is expected to dominate the light−matter interaction. Such a dipole coupling through Coulomb interactions among constituent AuNPs creates a continuum of collective plasmon modes in the superlattice.[7,21] Excitation of such collective resonant plasmon modes in the superlattice is responsible for the observed multiple resonance bands in the spectral response, similar to what has been reported in earlier works of AuSLs assembled with larger-size nanospheres.[7,21] We carried out full 3D numerical simulations (Supporting
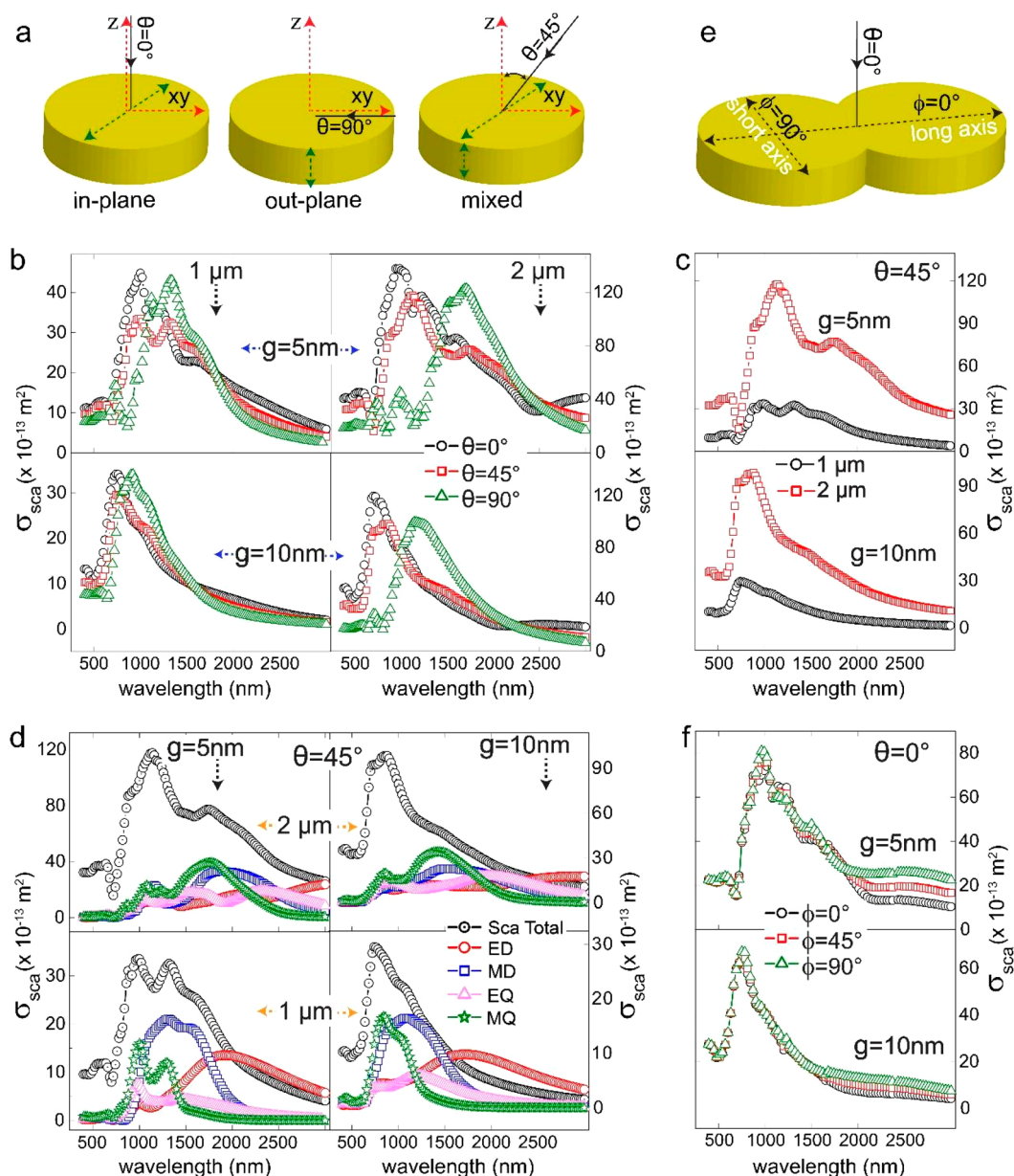
Figure 4. Numerical simulations. (a) Schematic of model geometry under different light incident conditions for exciting in-plane ($\theta = 0°$), out-of-plane ($\theta = 90°$), and mixed ($\theta = 45°$) modes of the superlattice. (b) Corresponding simulated scattering cross section spectra for superlattice sizes of 1 and 2 μm with 5 nm gap and 10 nm gap ($n_{inc} = 1.5$) effective index values. (c) Same as (b) but for only for $\theta = 45°$ (mixed mode) incident. The spectra undergo a red shift for the larger-size superlattice and smaller interparticle gap effective index value. (d) Multipole decomposition corresponding to $\theta = 45°$ (mixed mode) incident showing contributions of electric dipole (ED), magnetic dipole (MD), electric quadrupole (EQ), and magnetic quadrupole (MQ) for superlattice sizes of 1 and 2 μm with 5 nm gap and 10 nm gap ($n_{inc} = 1.5$) effective index values. (e) Schematic of model geometry under normal incident ($\theta = 0°$) for different light polarization directions. (f) Corresponding simulated scattering cross section spectra with 5 nm gap and 10 nm gap ($n_{inc} = 1.5$) effective index values.

Information, section S8) based on finite-element methods for more physical insight on the nature of the spectral response of our AuSL crystals. For simplicity, we assumed our AuSL to be cylindrical in shape, lying in the $x−y$ plane and suspended in air. A comparison with a more realistic rhombic dodecahedron-shaped crystal is presented in Figure S13, Supporting Information, and shows that the simplified cylindrical geometry provides a good approximation. Experimentally determined values of crystallite size (diameter between 1 and 2 μm) and fixed thickness (500 nm) were adopted for the cylinder. Effective optical constants were used for the superlattice material inside the model cylinder. These

constants were determined using an effective medium approach[66] (Supporting Information, section S8). Taking into consideration the length of the DNA strand used during AuSL synthesis as well the partial collapse of the microcrystals during drying, we estimated the interparticle spacing (edge to edge) to be between 5 and 10 nm. The presence of DNA was included as an effective medium with refractive index, n_{inc}, ranging between 1 (air) and 1.5, as discussed in Supporting Information Figure S11.

The scattering cross section for an isolated AuSL was calculated for three different plane wave illumination geometries, as illustrated in Figure 4a, corresponding to (i)
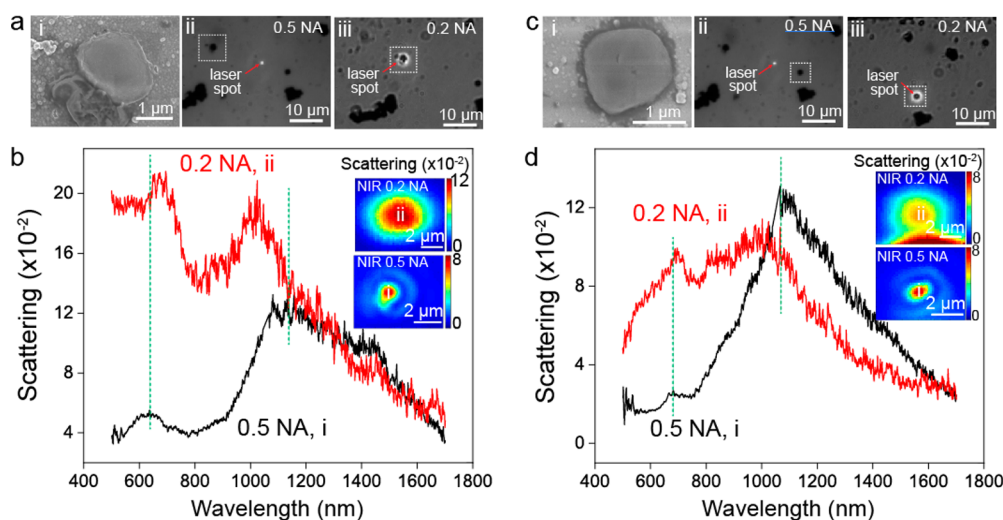
Figure 5. Dependence on the illumination geometry. (a) SEM (i) and bright-field transmission (ii,iii) images of a AuSL under 0.5 NA (ii) and 0.2 NA (iii) excitations. Bright spots in (ii) and (iii) represent laser spot size. (b) Corresponding scattering spectra under 0.5 and 0.2 NA excitations at the coordinates (i) and (ii) marked in the NIR hyperspectral maps (inset). The NIR maps are integrated over 850−1650 nm and are for vertically (0°) polarized light (c,d), same as (a,b) but for a different AuSL.

illumination from the top ($\theta = 0°$) with E-field polarized along the cylinder diameter, exiting in-plane modes; (ii) illumination from the side ($\theta = 90°$) with E-field polarized along the cylinder axis, exiting out-of-plane modes; (iii) illumination at $\theta = 45°$ exciting mix of both in-plane and out-of-plane modes. It was found that the presence of the AZO layer and glass substrate does not have a major impact on the resonance modes of the superlattice (Supporting Information, Figure S12).

Figure 4b shows the simulated scattering spectra for four combinations of superlattice diameters of 1 and 2 μm, gaps of 5 and 10 nm, all with a height of 500 nm and $n_{inc} = 1.5$. The scattering spectra show the main resonance modes peaking in the NIR and tailing off to longer wavelengths, in general agreement with the behavior seen experimentally.

Coupling to out-of-plane modes results in a red-shifted response seen for $\theta = 90°$; however, for illumination conditions as in our experiment, the effect of out-of-plane modes is moderate, as seen for $\theta = 45°$. The modes are red-shifted for smaller interparticle gap (i.e., higher effective index) and for larger AuSL crystal size, as expected for typical Mie resonant nanostructures,[67,68] however, much less than expected on the basis of geometric scaling of the crystal size. Figure 4c shows the dependence on crystal diameter for the $\theta = 45°$ incident mixed mode. Multipole decomposition[69,70] was carried out for the $\theta = 45°$ incident mixed mode, shown in Figure 4d, revealing the nature of the main resonance modes to be a mixture of overlapped higher multipoles. Electric dipole (ED) modes are more red-shifted for both 1 and 2 μm diameter AuSLs and do not contribute much to the main scattering peak. Instead, it is mostly a mixture of overlapped electric (EQ) and magnetic (MQ) quadrupole modes and partly magnetic dipoles (MD) that contribute to the main resonance modes for 1 μm diameter AuSL, and even more higher-order modes are expected to be the dominant contributions to the main resonance modes for the 2 μm diameter AuSL. Such an overlap of higher multipoles over an extended wavelength range could also further explain the broad spectral nature of our experimentally measured scattering spectra.

To explore the insensitivity of the experimental scattering response toward the polarization of the input light for even more anisotropic assemblies, we carried out additional simulations where the constant diameter cylinder was replaced by an asymmetric shape (see Figure 4e for schematics) consisting of two fused AuSLs with a long axis of 2 μm and a short axis of 1 μm but keeping the overall thickness at 500 nm. Figure 4f shows the simulated scattering cross section for the $\theta = 0°$ incident with polarizations along the short axis ($\phi = 90°$), long axis ($\phi = 0°$), and between ($\phi = 45°$). As seen, the scattering spectra overlap for all polarizations and hardly show any variations for the main resonances apart from an effect at long wavelengths corresponding to the ED mode. Such a polarization insensitivity of the resonance modes in AuSLs is also consistent with the highly multipolar nature of the scattering which inherently has weak dependence on input polarization.

To reveal the microscopic nature of the resonant modes in the AuSLs at the level of the individual AuNPs, we performed a limited number of full 3D numerical simulations, which are presented in Figure S14, Supporting Information. Here, the response of an AuSL of 20 AuNPs in each dimension (total of 8000 AuNPs) was simulated showing qualitative response in agreement with our observations. Electromagnetic near-field maps reveal the strong local field enhancement around individual AuNPs due to their dipole oscillation as well as the larger-scale mode structure over the entire AuSL corresponding to the geometric Mie resonances of the crystal.

To further explore the extent of out-of-plane mode contributions, we changed the illumination configuration in our dark-field setup to that shown in Figure 1b, where a 0.2 NA objective was used combined with a central beam stop in the transmission. The low-NA illumination contributes mostly normally incident light and therefore excites mostly the in-plane modes. Figure 5 shows a direct comparison of the measured scattering spectra of selected AuSL crystals for the two illumination conditions. For 0.2 NA excitation, the shorter wavelength scattering shows a large increase in magnitude but maintains its spectral position, while the longer wavelength main resonance mode undergoes a small blue shift. A red shift

of the main scattering peak with increasing angle of illumination agrees well with simulation results in Figure 4b, which suggests that scattering spectra measured with 0.5 NA excitation could have weak contributions from the out-of-plane resonances. We note that some of the increase in magnitude for the shorter wavelength resonance mode when using the 0.2 NA excitation geometry may be furthermore attributed to contributions from debris surrounding the AuSLs (see SEM images), which is more effectively suppressed when using the more tightly focused 0.5 NA geometry.

CONCLUSIONS

In conclusion, we have experimentally investigated the visible and near-infrared optical response of individual three-dimensional plasmonic crystals obtained through DNA-mediated assembly of Au nanospheres into closely packed superlattices. Hyperspectral mapping of these superlattices at the single-crystal level reveals a polarization-insensitive optical response with absorption dominating mostly in the visible range, while strong scattering occurs in the near-infrared range. Excitation of collective plasmonic supermodes due to dipole coupling, mediated by the Coulomb interactions among individual spherical NPs in the crystal, accounts for their characteristic optical response. Numerical simulations based on an effective medium approach reveal the main Mie resonances of the AuSLs, which can be attributed to higher-order multipoles. The crystals display good stability and robustness over time and could be measured several times within a period of weeks with little drift. Our work unambiguously shows the effective Mie resonances of these structures in a spectral range lying between the strong polaritonic response in the visible region and the dispersion-less effective dielectric regime in the far-infrared and provides an important foundation for exploiting these materials in a range of future applications. The characteristic structural and optical properties of AuSLs may be of interest for applications in the field of thermoplasmonics, photocatalysis, biochemical sensing, surface-enhanced Raman scattering, nonlinear optics, and potentially as strongly scattering materials for complex nanophotonics. While the microscopic origin of dipole−dipole coupling in our present crystal assembled with small-size spherical nanoparticles is not as strong as the capacitive coupling seen in crystals with large-size nanocubes, a significant amount of near-field is expected to exist in the nanogaps between the nanoparticles, which may be exploited for nonlinear optics and sensing in future studies.

ASSOCIATED CONTENT

Data Availability Statement

All data supporting this study are openly available from the University of Southampton repository (DOI: 10.5258/SOTON/D2368).

ⓈI Supporting Information

The Supporting Information is available free of charge at https://pubs.acs.org/doi/10.1021/acsaom.2c00008.

> Methods and materials for sample synthesis and characterization; optical characterization; details of the numerical simulations (PDF)

AUTHOR INFORMATION

Corresponding Authors

Otto L. Muskens − *Physics and Astronomy, Faculty of Engineering and Physical Sciences and Institute for Life Sciences, University of Southampton, SO17 1BJ Southampton, United Kingdom;* ⓞ orcid.org/0000-0003-0693-5504; Email: o.muskens@soton.ac.uk

Antonios G. Kanaras − *Physics and Astronomy, Faculty of Engineering and Physical Sciences and Institute for Life Sciences, University of Southampton, SO17 1BJ Southampton, United Kingdom;* ⓞ orcid.org/0000-0002-9847-6706; Email: a.kanaras@soton.ac.uk

Authors

Haobijam Johnson Singh − *Physics and Astronomy, Faculty of Engineering and Physical Sciences, University of Southampton, SO17 1BJ Southampton, United Kingdom*

Doxi Misatziou − *Physics and Astronomy, Faculty of Engineering and Physical Sciences, University of Southampton, SO17 1BJ Southampton, United Kingdom;* ⓞ orcid.org/0000-0002-3798-9866

Callum Wheeler − *Electrical Engineering and Computer Science, Faculty of Engineering and Physical Sciences, University of Southampton, SO17 1BJ Southampton, United Kingdom*

Álvaro Buendía − *Instituto de Estructura de la Materia (IEM), Consejo Superior de Investigaciones Científicas (CSIC), 28006 Madrid, Spain*

Vincenzo Giannini − *Instituto de Estructura de la Materia (IEM), Consejo Superior de Investigaciones Científicas (CSIC), 28006 Madrid, Spain; Technology Innovation Institute, Abu Dhabi, United Arab Emirates; Centre of Excellence ENSEMBLE3 sp. z o.o., Warsaw 01-919, Poland;* ⓞ orcid.org/0000-0001-8025-4964

José A. Sánchez-Gil − *Instituto de Estructura de la Materia (IEM), Consejo Superior de Investigaciones Científicas (CSIC), 28006 Madrid, Spain;* ⓞ orcid.org/0000-0002-5370-3717

Martinus H. V. Werts − *Univ. Rennes, CNRS, SATIE−UMR 8029, F-35000 Rennes, France; École normale supérieure de Rennes, F-35170 Bruz, France;* ⓞ orcid.org/0000-0003-1965-8876

Tom Brown − *Chemistry Research Laboratory, Department of Chemistry, University of Oxford, Oxford OX1 3TA, United Kingdom;* ⓞ orcid.org/0000-0002-6538-3036

Afaf H. El-Sagheer − *Chemistry Research Laboratory, Department of Chemistry, University of Oxford, Oxford OX1 3TA, United Kingdom; Chemistry Branch, Department of Science and Mathematics, Faculty of Petroleum and Mining Engineering, Suez University, Suez 43721, Egypt;* ⓞ orcid.org/0000-0001-8706-1292

Complete contact information is available at:
https://pubs.acs.org/10.1021/acsaom.2c00008

Notes

The authors declare no competing financial interest.

■ REFERENCES

(1) Wang, L.; Hasanzadeh Kafshgari, M.; Meunier, M. Optical Properties and Applications of Plasmonic-Metal Nanoparticles. *Adv. Funct. Mater.* **2020**, *30* (51), 2005400.

(2) Yang, P.; Zheng, J.; Xu, Y.; Zhang, Q.; Jiang, L. Colloidal Synthesis and Applications of Plasmonic Metal Nanoparticles. *Adv. Mater.* **2016**, *28* (47), 10508−10517.

(3) Maier, S. A. *Plasmonics: Fundamentals and Applications*, 1st ed.; Springer: New York, NY, 2007.

(4) Baumberg, J. J.; Aizpurua, J.; Mikkelsen, M. H.; Smith, D. R. Extreme Nanophotonics from Ultrathin Metallic Gaps. *Nat. Mater.* **2019**, *18* (7), 668−678.

(5) Schuller, J. A.; Barnard, E. S.; Cai, W.; Jun, Y. C.; White, J. S.; Brongersma, M. L. Plasmonics for Extreme Light Concentration and Manipulation. *Nat. Mater.* **2010**, *9* (3), 193−204.

(6) Gwo, S.; Chen, H. Y.; Lin, M. H.; Sun, L.; Li, X. Nanomanipulation and Controlled Self-Assembly of Metal Nanoparticles and Nanocrystals for Plasmonics. *Chem. Soc. Rev.* **2016**, *45* (20), 5672−5716.

(7) Mueller, N. S.; Okamura, Y.; Vieira, B. G. M.; Juergensen, S.; Lange, H.; Barros, E. B.; Schulz, F.; Reich, S. Deep Strong Light−Matter Coupling in Plasmonic Nanoparticle Crystals. *Nature* **2020**, *583* (7818), 780−784.

(8) Wang, D.; Guan, J.; Hu, J.; Bourgeois, M. R.; Odom, T. W. Manipulating Light-Matter Interactions in Plasmonic Nanoparticle Lattices. *Acc. Chem. Res.* **2019**, *52* (11), 2997−3007.

(9) Mayer, M.; Schnepf, M. J.; Konig, T. A. F.; Fery, A. Colloidal Self-Assembly Concepts for Plasmonic Metasurfaces. *Adv. Opt. Mater.* **2019**, *7* (1), 1800564.

(10) Liberal, I.; Engheta, N. Near-Zero Refractive Index Photonics. *Nat. Photonics* **2017**, *11* (3), 149−158.

(11) Diroll, B. T.; Guo, P.; Chang, R. P. H.; Schaller, R. D. Large Transient Optical Modulation of Epsilon-Near-Zero Colloidal Nanocrystals. *ACS Nano* **2016**, *10* (11), 10099−10105.

(12) Pollard, R. J.; Murphy, A.; Hendren, W. R.; Evans, P. R.; Atkinson, R.; Wurtz, G. A.; Zayats, A. V.; Podolskiy, V. A. Optical Nonlocalities and Additional Waves in Epsilon-near-Zero Metamaterials. *Phys. Rev. Lett.* **2009**, *102* (12), 127405.

(13) Urzhumov, Y. A.; Shvets, G.; Fan, J. A.; Capasso, F.; Brandl, D.; Nordlander, P. Plasmonic Nanoclusters: A Path towards Negative-Index Metafluids. *Opt. Express* **2007**, *15* (21), 14129−14145.

(14) Fruhnert, M.; Mühlig, S.; Lederer, F.; Rockstuhl, C. Towards Negative Index Self-Assembled Metamaterials. *Phys. Rev. B - Condens. Matter Mater. Phys.* **2014**, *89* (7), 075408.

(15) Park, D. J.; Zhang, C.; Ku, J. C.; Zhou, Y.; Schatz, G. C.; Mirkin, C. A. Plasmonic Photonic Crystals Realized through DNA-Programmable Assembly. *Proc. Natl. Acad. Sci. U. S. A.* **2015**, *112* (4), 977−981.

(16) Kuzyk, A.; Schreiber, R.; Fan, Z.; Pardatscher, G.; Roller, E.-M.; Högele, A.; Simmel, F. C.; Govorov, A. O.; Liedl, T. DNA-Based Self-Assembly of Chiral Plasmonic Nanostructures with Tailored Optical Response. *Nature* **2012**, *483* (7389), 311−314.

(17) Hentschel, M.; Schäferling, M.; Duan, X.; Giessen, H.; Liu, N. Chiral Plasmonics. *Sci. Adv.* **2017**, *3* (5), e1602735.

(18) Collins, J. T.; Kuppe, C.; Hooper, D. C.; Sibilia, C.; Centini, M.; Valev, V. K. Chirality and Chiroptical Effects in Metal Nanostructures: Fundamentals and Current Trends. *Adv. Opt. Mater.* **2017**, *5* (16), 1700182.

(19) Wu, W.; Pauly, M. Chiral Plasmonic Nanostructures: Recent Advances in Their Synthesis and Applications. *Mater. Adv.* **2022**, *3* (1), 186−215.

(20) Langer, J.; Jimenez de Aberasturi, D.; Aizpurua, J.; Alvarez-Puebla, R. A.; Auguie, B.; Baumberg, J. J.; Bazan, G. C.; Bell, S. E. J.; Boisen, A.; Brolo, A. G.; Choo, J.; Cialla-May, D.; Deckert, V.; Fabris, L.; Faulds, K.; Garcia de Abajo, F. J.; Goodacre, R.; Graham, D.; Haes, A. J.; Haynes, C. L.; Huck, C.; Itoh, T.; Kall, M.; Kneipp, J.; Kotov, N. A.; Kuang, H.; Le Ru, E. C.; Lee, H. K.; Li, J.-F.; Ling, X. Y.; Maier, S. A.; Mayerhofer, T.; Moskovits, M.; Murakoshi, K.; Nam, J.-M.; Nie, S.; Ozaki, Y.; Pastoriza-Santos, I.; Perez-Juste, J.; Popp, J.; Pucci, A.; Reich, S.; Ren, B.; Schatz, G. C.; Shegai, T.; Schlucker, S.; Tay, L.-L.; Thomas, K. G.; Tian, Z.-Q.; Van Duyne, R. P.; Vo-Dinh, T.; Wang, Y.; Willets, K. A.; Xu, C.; Xu, H.; Xu, Y.; Yamamoto, Y. S.; Zhao, B.; Liz-Marzan, L. M. Present and Future of Surface-Enhanced Raman Scattering. *ACS Nano* **2020**, *14* (1), 28−117.

(21) Turek, V. A.; Francescato, Y.; Cadinu, P.; Crick, C. R.; Elliott, L.; Chen, Y.; Urland, V.; Ivanov, A. P.; Velleman, L.; Hong, M.; Vilar, R.; Maier, S. A.; Giannini, V.; Edel, J. B. Self-Assembled Spherical Supercluster Metamaterials from Nanoscale Building Blocks. *ACS Photonics* **2016**, *3* (1), 35−42.

(22) Mann, M. E.; Yadav, P.; Kim, S. Colloidal Plasmonic Nanocubes as Capacitor Building Blocks for Multidimensional Optical Metamaterials: A Review. *ACS Appl. Nano Mater.* **2021**, *4* (10), 9976−9984.

(23) Kauranen, M.; Zayats, A. V. Nonlinear Plasmonics. *Nat. Photonics* **2012**, *6* (11), 737−748.

(24) Butet, J.; Brevet, P. F.; Martin, O. J. F. Optical Second Harmonic Generation in Plasmonic Nanostructures: From Fundamental Principles to Advanced Applications. *ACS Nano* **2015**, *9* (11), 10545−10562.

(25) Wang, Z.; Meng, X.; Kildishev, A. V.; Boltasseva, A.; Shalaev, V. M. Nanolasers Enabled by Metallic Nanoparticles: From Spasers to Random Lasers. *Laser Photon. Rev.* **2017**, *11* (6), 1700212.

(26) Soukoulis, C. M.; Wegener, M. Past Achievements and Future Challenges in the Development of Three-Dimensional Photonic Metamaterials. *Nat. Photonics* **2011**, *5* (9), 523−530.

(27) Jung, C.; Kim, G.; Jeong, M.; Jang, J.; Dong, Z.; Badloe, T.; Yang, J. K. W.; Rho, J. Metasurface-Driven Optically Variable Devices. *Chem. Rev.* **2021**, *121* (21), 13013−13050.

(28) Tanaka, T.; Ishikawa, A. Towards Three-Dimensional Optical Metamaterials. *Nano Converg.* **2017**, *4* (1), 34.

(29) Hong, Y. H.; Hsu, W. C.; Tsai, W. C.; Huang, Y. W.; Chen, S. C.; Kuo, H. C. Ultracompact Nanophotonics: Light Emission and Manipulation with Metasurfaces. *Nanoscale Res. Lett.* **2022**, *17* (1), 41.

(30) Zhu, Y.; Tang, T.; Zhao, S.; Joralmon, D.; Poit, Z.; Ahire, B.; Keshav, S.; Raje, A. R.; Blair, J.; Zhang, Z.; Li, X. Recent Advancements and Applications in 3D Printing of Functional Optics. *Addit. Manuf.* **2022**, *52*, 102682.

(31) Baig, N.; Kammakakam, I.; Falath, W. Nanomaterials: A Review of Synthesis Methods, Properties, Recent Progress, and Challenges. *Mater. Adv.* **2021**, *2* (6), 1821−1871.

(32) Mirkin, C. A.; Letsinger, R. L.; Mucic, R. C.; Storhoff, J. J. A DNA-Based Method for Rationally Assembling Nanoparticles into Macroscopic Materials. *Nature* **1996**, *382*, 607−609.

(33) Nykypanchuk, D.; Maye, M. M.; Van Der Lelie, D.; Gang, O. DNA-Guided Crystallization of Colloidal Nanoparticles. *Nature* **2008**, *451* (7178), 549−552.

(34) Park, S. Y.; Lytton-Jean, A. K. R.; Lee, B.; Weigand, S.; Schatz, G. C.; Mirkin, C. A. DNA-Programmable Nanoparticle Crystallization. *Nature* **2008**, *451* (7178), 553−556.

(35) Laramy, C. R.; O'Brien, M. N.; Mirkin, C. A. Crystal Engineering with DNA. *Nat. Rev. Mater.* **2019**, *4* (3), 201−224.

(36) Huh, J. H.; Kim, K.; Im, E.; Lee, J.; Cho, Y. D.; Lee, S. Exploiting Colloidal Metamaterials for Achieving Unnatural Optical Refractions. *Adv. Mater.* **2020**, *32* (51), 2001806.

(37) Ross, M. B.; Blaber, M. G.; Schatz, G. C. Using Nanoscale and Mesoscale Anisotropy to Engineer the Optical Response of Three-Dimensional Plasmonic Metamaterials. *Nat. Commun.* **2014**, *5*, 4090.

(38) Kim, S.; Zheng, C. Y.; Schatz, G. C.; Aydin, K.; Kim, K. H.; Mirkin, C. A. Mie-Resonant Three-Dimensional Metacrystals. *Nano Lett.* **2020**, *20* (11), 8096−8101.

(39) Young, K. L.; Ross, M. B.; Blaber, M. G.; Rycenga, M.; Jones, M. R.; Zhang, C.; Senesi, A. J.; Lee, B.; Schatz, G. C.; Mirkin, C. A. Using DNA to Design Plasmonic Metamaterials with Tunable Optical Properties. *Adv. Mater.* **2014**, *26* (4), 653−659.

(40) Sun, L.; Lin, H.; Kohlstedt, K. L.; Schatz, G. C.; Mirkin, C. A. Design Principles for Photonic Crystals Based on Plasmonic Nanoparticle Superlattices. *Proc. Natl. Acad. Sci. U. S. A.* **2018**, *115* (28), 7242−7247.

(41) Tapio, K.; Bald, I. The Potential of DNA Origami to Build Multifunctional Materials. *Multifunct. Mater.* **2020**, *3* (3), 032001.

(42) De Fazio, A. F.; Misatziou, D.; Baker, Y. R.; Muskens, O. L.; Brown, T.; Kanaras, A. G. Chemically Modified Nucleic Acids and DNA Intercalators as Tools for Nanoparticle Assembly. *Chem. Soc. Rev.* **2021**, *50* (23), 13410−13440.

(43) Seo, S. E.; Girard, M.; Olvera de la Cruz, M.; Mirkin, C. A. Non-Equilibrium Anisotropic Colloidal Single Crystal Growth with DNA. *Nat. Commun.* **2018**, *9*, 4558.

(44) Jones, M. R.; MacFarlane, R. J.; Lee, B.; Zhang, J.; Young, K. L.; Senesi, A. J.; Mirkin, C. A. DNA-Nanoparticle Superlattices Formed from Anisotropic Building Blocks. *Nat. Mater.* **2010**, *9* (11), 913−917.

(45) Xiong, H.; Sfeir, M. Y.; Gang, O. Assembly, Structure and Optical Response of Three-Dimensional Dynamically Tunable Multicomponent Superlattices. *Nano Lett.* **2010**, *10* (11), 4456−4462.

(46) Sun, D.; Gang, O. Binary Heterogeneous Superlattices Assembled from Quantum Dots and Gold Nanoparticles with DNA. *J. Am. Chem. Soc.* **2011**, *133* (14), 5252−5254.

(47) Lu, F.; Yager, K. G.; Zhang, Y.; Xin, H.; Gang, O. Superlattices Assembled through Shape-Induced Directional Binding. *Nat. Commun.* **2015**, *6*, 6912.

(48) Meyer, T. A.; Zhang, C.; Bao, G.; Ke, Y. Programmable Assembly of Iron Oxide Nanoparticles Using DNA Origami. *Nano Lett.* **2020**, *20* (4), 2799−2805.

(49) De Fazio, A. F.; Haines, J.; Courtier, A.; Muskens, O. L.; Kanaras, A. G. Optical Response of Gold and Upconversion Nanoparticles Assembled via DNA Interaction. *Proc. SPIE* **2019**, *10892*, 108920A.

(50) Kahn, J. S.; Gang, O. Designer Nanomaterials through Programmable Assembly. *Angew. Chemie - Int. Ed.* **2022**, *61*, e202105678.

(51) Choi, J.-H.; Wang, H.; Oh, S. J.; Paik, T.; Sung, P.; Sung, J.; Ye, X.; Zhao, T.; Diroll, B. T.; Murray, C. B.; Kagan, C. R. Exploiting the Colloidal Nanocrystal Library to Construct Electronic Devices. *Science* **2016**, *352* (6282), 205−208.

(52) Yamada, Y.; Tsung, C. K.; Huang, W.; Huo, Z.; Habas, S. E.; Soejima, T.; Aliaga, C. E.; Somorjai, G. A.; Yang, P. Nanocrystal Bilayer for Tandem Catalysis. *Nat. Chem.* **2011**, *3* (5), 372−376.

(53) Nicoli, F.; Zhang, T.; Hübner, K.; Jin, B.; Selbach, F.; Acuna, G.; Argyropoulos, C.; Liedl, T.; Pilo-Pais, M. DNA-Mediated Self-Assembly of Plasmonic Antennas with a Single Quantum Dot in the Hot Spot. *Small* **2019**, *15* (26), 1804418.

(54) Sun, D.; Tian, Y.; Zhang, Y.; Xu, Z.; Sfeir, M. Y.; Cotlet, M.; Gang, O. Light-Harvesting Nanoparticle Core-Shell Clusters with Controllable Optical Output. *ACS Nano* **2015**, *9* (6), 5657−5665.

(55) Rockstuhl, C.; Lederer, F.; Etrich, C.; Pertsch, T.; Scharf, T. Design of an Artificial Three-Dimensional Composite Metamaterial with Magnetic Resonances in the Visible Range of the Electromagnetic Spectrum. *Phys. Rev. Lett.* **2007**, *99* (1), 017401.

(56) Hooshmand, N.; Bordley, J. A.; El-sayed, M. A. Are Hot Spots between Two Plasmonic Nanocubes of Silver or Gold Formed between Adjacent Corners or Adjacent Facets? A DDA Examination. *J. Phys. Chem. Lett.* **2014**, *5*, 2229−2234.

(57) Grillet, N.; Manchon, D.; Bertorelle, F.; Bonnet, C.; Broyer, M.; Cottancin, E.; Lermé, J.; Hillenkamp, M.; Pellarin, M. Plasmon Coupling in Silver Nanocube Dimers: Resonance Splitting Induced by Edge Rounding. *ACS Nano* **2011**, *5* (12), 9450−9462.

(58) Roth, G. A.; Tahiliani, S.; Neu-Baker, N. M.; Brenner, S. A. Hyperspectral Microscopy as an Analytical Tool for Nanomaterials. *Wiley Interdiscip. Rev. Nanomedicine Nanobiotechnology* **2015**, *7* (4), 565−579.

(59) Auyeung, E.; Li, T. I. N. G.; Senesi, A. J.; Schmucker, A. L.; Pals, B. C.; De La Cruz, M. O.; Mirkin, C. A. DNA-Mediated Nanoparticle Crystallization into Wulff Polyhedra. *Nature* **2014**, *505* (7481), 73−77.

(60) Seo, S. E.; Wang, M. X.; Shade, C. M.; Rouge, J. L.; Brown, K. A.; Mirkin, C. A. Modulating the Bond Strength of DNA-Nanoparticle Superlattices. *ACS Nano* **2016**, *10* (2), 1771−1779.

(61) Oh, T.; Ku, J. C.; Lee, J. H.; Hersam, M. C.; Mirkin, C. A. Density-Gradient Control over Nanoparticle Supercrystal Formation. *Nano Lett.* **2018**, *18* (9), 6022−6029.

(62) Oh, T.; Park, S. S.; Mirkin, C. A. Stabilization of Colloidal Crystals Engineered with DNA. *Adv. Mater.* **2019**, *31* (1), 1805480.

(63) De Fazio, A. F.; El-Sagheer, A. H.; Kahn, J. S.; Nandhakumar, I.; Burton, M. R.; Brown, T.; Muskens, O. L.; Gang, O.; Kanaras, A. G. Light-Induced Reversible DNA Ligation of Gold Nanoparticle Superlattices. *ACS Nano* **2019**, *13* (5), 5771−5777.

(64) Harimech, P. K.; Gerrard, S. R.; El-Sagheer, A. H.; Brown, T.; Kanaras, A. G. Reversible Ligation of Programmed DNA-Gold Nanoparticle Assemblies. *J. Am. Chem. Soc.* **2015**, *137* (29), 9242−9245.

(65) Neil, M. A. A.; Juškaitis, R.; Wilson, T.; Sarafis, V.; Laczik, Z. J. Optimized Pupil-Plane Filters for Confocal Microscope Point-Spread Function Engineering. *Opt. Lett.* **2000**, *25* (4), 245−247.

(66) Palmer, S. J.; Xiao, X.; Pazos-Perez, N.; Guerrini, L.; Correa-Duarte, M. A.; Maier, S. A.; Craster, R. V.; Alvarez-Puebla, R. A.; Giannini, V. Extraordinarily Transparent Compact Metallic Metamaterials. *Nat. Commun.* **2019**, *10*, 2118.

(67) Kuznetsov, A. I.; Miroshnichenko, A. E.; Brongersma, M. L.; Kivshar, Y. S.; Luk'yanchuk, B. Optically Resonant Dielectric Nanostructures. *Science* **2016**, *354* (6314), aag2472.

(68) Jahani, S.; Jacob, Z. All-Dielectric Metamaterials. *Nat. Nanotechnol.* **2016**, *11*, 23−36.

(69) Evlyukhin, A. B.; Fischer, T.; Reinhardt, C.; Chichkov, B. N. Optical Theorem and Multipole Scattering of Light by Arbitrarily Shaped Nanoparticles. *Phys. Rev. B* **2016**, *94* (20), 205434.

(70) Evlyukhin, A. B.; Chichkov, B. N. Multipole Decompositions for Directional Light Scattering. *Phys. Rev. B* **2019**, *100* (12), 125415.